Available online at www.sciencedirect.com
SCIENCE DIRECT®
Journal of Nuclear Materials 327 (2004) 11–18
journal of nuclear materials
www.elsevier.com/locate/jnucmat

# A new method to study hydriding processes from the inner surfaces of fuel claddings

J.L. Sacedón [a,*], M. Díaz [a], J.S. Moya [a], B. Remartínez [b], J. Izquierdo [b]

[a] *Instituto de Ciencia de Materiales de Madrid (CSIC), Cantoblanco, Madrid 28049, Spain*
[b] *TEMAT Iberdrola, Po Virgen del Puerto, Madrid 28005, Spain*

Received 24 March 2003; accepted 7 January 2004

**Abstract**

In this paper, a new method that allows the study of the hydriding process of fuel claddings from the inner surfaces is presented. The hydriding is performed by heating the cladding in an ultra-high vacuum chamber while hydrogen flows inside the tube. The external $H_2$ partial pressure, the tube electrical resistance and the power dissipated by the reaction are measured throughout the process. These measurements at different hydriding stages are complemented with an optical microscopy analysis of the claddings give insight into the main physical processes. As a consequence a description of the hydriding first stages is provided. The method allows the measurement of the incubation and failure times and the total energy dissipated by the hydriding reaction.


*PACS:* 28.41.Bm; 28.90.+i

## 1. Introduction

The tube burst technique has been recently applied to study the hydriding of fuel claddings inner surfaces [1], the results obtained are complementary to those from thermogravimetric methods [2,3]. This method, as well as the use of heat interchangers [4] or miniboilers, exhibits the advantage that experiments (study of properties and testing) can be performed on industrial components maintaining their geometry and structure. The hydriding process on long industrial samples, with the reaction starting from the tube inner surface, is especially appropriate because it provides information on both the inner surface and bulk properties as well as on the reliability of the fabrication process.

Additionally, the cylindrical symmetry of the cladding is suitable to obtain basic knowledge on the hydride layer structure, on the reaction propagation front and on the hydride morphology in the remaining metallic zone. This geometry, in fact, facilitates a way to control the material exposed to hydrogen and to measure several important reaction parameters.

In the new method presented in this paper [5,6], the cladding is inserted in an ultra-high vacuum (UHV) chamber. This environment makes it possible to measure different parameters, such as the external $H_2$ partial pressure, the resistivity and the power dissipated by the hydriding reaction, named from now on as the hydriding dissipated power (HDP). The integration of the dissipated power curve versus time will be named the hydriding dissipated energy (HDE). These parameters are dependent on the hydriding stages, allowing the determination of incubation and failure times. The tube failure has been experimentally defined as the abrupt loss of the $H_2$ sealing condition. This event is simultaneous with the occurrence of macroscopic deformations or crack initiations at the outer surface. The method can be used as a test of resistance to hydriding processes. This allows to compare different compositional and

* Corresponding author. Tel.: +34-91 334 9000; fax: +34-91 372 0623.
*E-mail address:* sacedon@icmm.csic.es (J.L. Sacedón).

0022-3115/$ - see front matter © 2004 Elsevier B.V. All rights reserved.
doi:10.1016/j.jnucmat.2004.01.001

structural cladding designs, such as bare surfaces, liners or protective coatings. The $H_2$ partial pressure is proportional to the square of hydrogen concentration at the external surface of the tube, assuming a second order desorption kinetics [7]. The resistance change makes it possible to follow the dissolution of H in the α-Zr phase, and the hydriding dissipated power allows the comparison of the reaction speed and stoichiometry variations during the process. In this regard, the purpose of this work is two-fold: first, to describe the reliability and performance of the developed testing method and second, to increase the knowledge on the hydriding process comparing the measured parameters with optical microscopy analyses of different cross-sections of the claddings at different stages.

## 2. Experimental

The scheme of the UHV chamber built for these experiments is illustrated in Fig. 1. The tube cladding is inserted in the chamber through two Swagelook™ vacuum tube fittings (with Viton gaskets and welded on 33 mm CF flanges). The tube is electrically isolated from the chamber using UHV tubular ceramic feed-troughs. One of the flanges is mounted on a flexible below to avoid mechanical stress during the thermal treatments. The cladding is heated by an applied alternating current to heat the cladding tube, requiring an intensity of 30 A to achieve an experiment reference temperature of 360 °C, with a distance of 50 cm between the heating electrodes. This configuration provides a temperature plateau of 25 cm in the central region. Two nickel wire rings are used to measure the electrical resistance. They are located 1.5 cm from the tube center, therefore drop voltage values are referred to a length of 3 cm. Three thermocouples are spot welded to the tube, one at the center (controlling the heating power to maintain the reference temperature at this point) and the other two are welded to the extremes of the heated length to assure, as much as possible, a symmetrical temperature distribution. It is important to note that the welding of thermocouples on the cladding is required to avoid errors in the temperature measurement. The optical micrographs show that this welding does not affect the hydriding process.

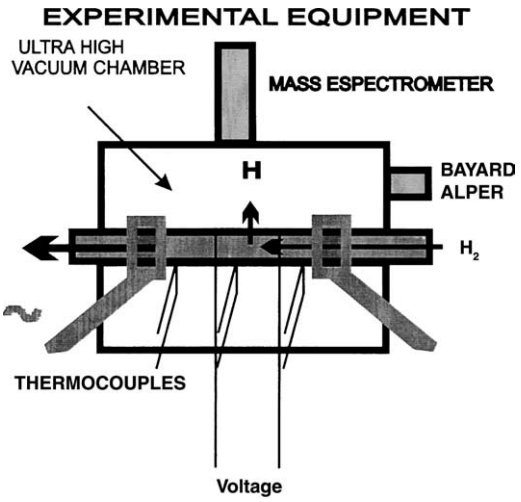


Fig. 1. Scheme of the experimental set up.

The main chamber is pumped by a 200 l/s turbo molecular pump (TMP). The $H_2$ line is built using high vacuum (HV) and UHV components and it is connected to the cladding tube. This line is pumped down to $2\times10^{-7}$ Torr by an auxiliary 80 l/s TMP. This pressure value implies a contaminant concentration lower than 10 ppm with a $H_2$ flux of 0.2 l/min. The experiments have been performed without any addition of water vapor. The hydrogen used is a commercial 6 N purity. The hydrogen line is kept in the low $10^{-7}$ Torr range during all the thermal processes prior to experiment itself. A quadruple mass spectrometer and a Bayard Alpert gauge are used to monitor partial and total pressures in the UHV chamber.

A customary bake out, 24 h at 190 °C, is run after the cladding tube mounting, reaching a pressure of $3\times10^{-10}$ Torr or lower in the UHV chamber. Afterwards, the cladding tube is out-gassed at 370 °C during 24 h. At the end of the out-gassing process, a pressure of $1\times10^{-9}$ Torr is reached with this temperature in the cladding. During the bake out the line pumping is confined to the cladding inner, and the pressure inside the tube rises from $10^{-8}$ to $10^{-7}$ Torr. This value is four orders of magnitude lower than the partial pressure of impurities contained in the 6N $H_2$ used for the experiment. Therefore, if an increase of the native oxide layer could be produced, the effect will not be higher than the expected from $H_2O$ impurities (<0.4 ppm) contained in the experiment gas. Before the hydriding experiment starts, the cladding tube is cooled down to less than 50 °C. Later, it is filled with $H_2$, the pressure equilibrated to 1 atm. and the $H_2$ flux stabilized to 0.2 l/min. The tube temperature is raised to the experiment reference value at a rate of 10 °C/min. The parameters recorded during the hydriding process are: heating current, voltage drop in the cladding central region, temperatures, pressures, $H_2$ flux and mass spectra. The control system cuts the heating power at a pressure $\geqslant 1\times10^{-6}$ Torr. In normal conditions this event occurs only when the tube sealing condition is abruptly lost, giving the failure time.

Hydride morphology was observed on chemical etched cross-sections with an acid solution ($H_2O_2$: $HNO_3$: HF = 20 ml: 20 ml: 4 ml), using an optical microscope (Leica, DMR model), after polishing down to 0.04 μm using a commercial suspension of colloidal silica.

A X-ray diffractometer (Siemens, D-5001) was used to identify the zirconium hydride phases formed at the inner surface. The specimens were sectioned into several pieces with dimensions about 5 mm in length and 2 mm width to make a plate formed by tiles suitable for X-ray analysis.

## 3. Results and discussion

Preliminary experiments were performed using a small equipment that assured a 6 cm temperature plateau in the central region of the samples, whose wall thickness was reduced to 0.4 mm. The samples were mainly used to study the morphology associated with the cladding failure. In these experiments, tubes with different inner surface finishing were tested and, in general, two kinds of hydriding processes were observed and related to the inner surface structure. The first type of behavior was observed when the inner surface ends in a smooth, near pure Zr liner, which consisted of relatively flat and large grains. In this case, the tube external surface suffers a deformation in the central region that appears to be associated with the formation of a circular hydride front. Fig. 2 illustrates the circular formation. In more detail, this figure shows radial hydride precipitates connecting the hydriding front with the external surface. The external surface exhibits important deformations and sometimes microcracks, but it does not show a clear longitudinal crack initiation. However, these samples were found to be very brittle and sometimes they crack transversally while they are dismounted.

It is known that the hydriding failures of Zircaloy frequently occur as 'sunburst-type' localized massive hydriding, forming a non-circular front as it is shown in the Fig. 9(a) of Ref. [2] for a Zircaloy-2 cladding. We have detected this pattern when the failure of the tube is produced outside of the temperature plateau, at a lower temperature than the reference temperature. This indicates that hydrogen takes advantage of any small inhomogeneity in the inner surface. Longitudinal microcracks are clearly seen in this configuration. Up until now, we have not detected this behavior in the lined samples.

Therefore, tubes with a liner present a more uniform behavior that makes them appropriate to test the capabilities of the system previously described and to provide some insight in the hydriding process. Four 84 cm length samples of Zircaloy-2 with nominal 0.6 mm wall thickness were used to study the reproducibility of the method. They correspond to two different batches and the experimental results show that all of them exhibit the same qualitative behavior and nearly the same values of failure times and total energy produced by the hydriding reaction. In addition to this set of experiments several partially hydrided tube claddings have been analyzed to study different stages of the hydriding process.

The heating power required to maintain the reference temperature (360 °C) in the 3 cm central region during the hydriding progress is plotted in Fig. 3. This figure shows that after the power ramp needed to attain the experiment reference temperature, the power stabilizes for a short interval and then it drops drastically. In absence of other phenomena, the power dissipation should be constant and it is mainly due to thermal emission from the outer surface. The nickel rings are positioned in the central plateau without temperature gradient and consequently the conduction losses along the cladding are not relevant in this zone. Another heat emission source corresponds to the inner surface radiation that can be simulated as a long black body. The

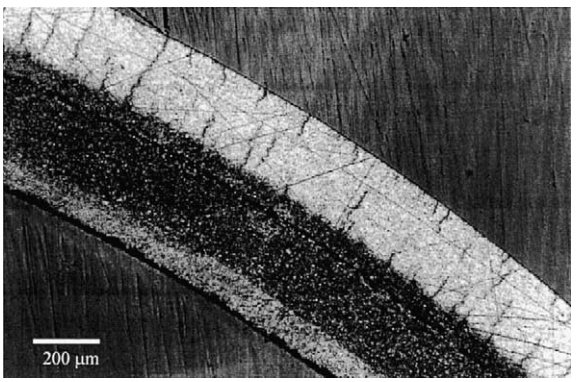


Fig. 2. Chemically etched Zircaloy-2 sample with inner liner showing the formation of a homogeneous hydride rim and the hydride precipitates growing in the radial direction.

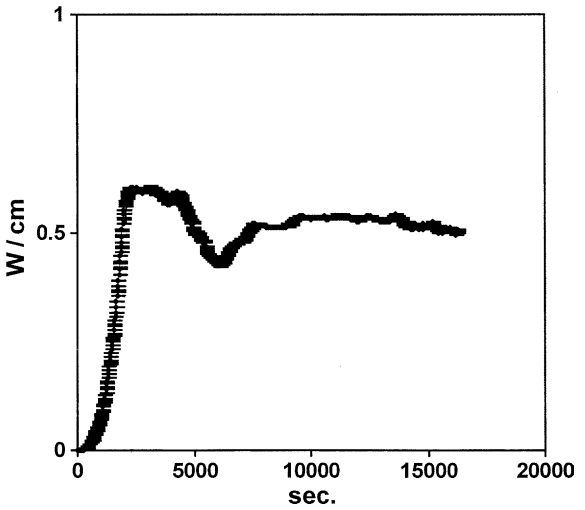


Fig. 3. Power supplied to the 3 cm cladding center to maintain a constant temperature of 360 °C during the hydriding.

energy emitted by the inner surface per unit length is estimated about 1/20th of the energy emitted from the outer surface. Heat transported by the $H_2$ flow is estimated to be two orders of magnitude lower than the total emission. Therefore, in absence of other phenomena the heating power equilibrates the power losses mainly due to radiation from the outer surface. However, sometime after the temperature stabilizes, a drop in the power needed to maintain the temperature is observed. This drop is detailed in Fig. 4 and its time integral is shown in Fig. 5. It is interesting to compare the results shown in Fig. 4 with the kinetic curve obtained in an hydriding experiment of $LaNi_5$ (on a single circular surface) [8]. The HDE curve (Fig. 5) seems similar to the

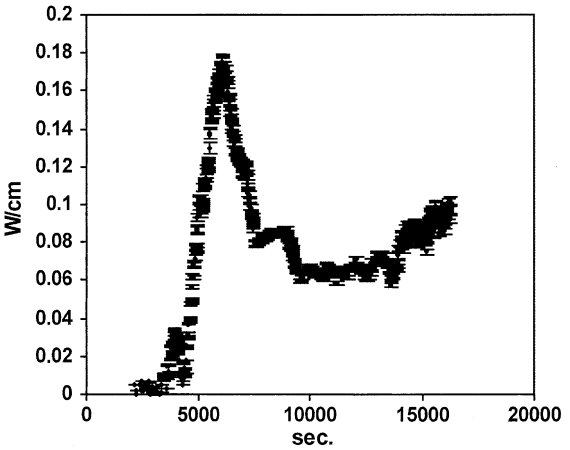


Fig. 4. Defect of supplied power during the hydriding. This defect of power, is fulfilled by the hydriding reaction as consequence of the dissipated reaction heat. It is named in the text as hydriding dissipated power (HDP).

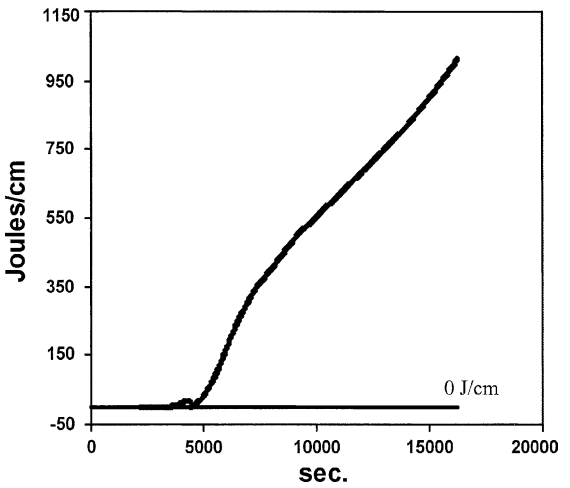


Fig. 5. Hydriding dissipated energy (HDE) during the hydriding reaction.

weight increase observed in thermogravimetry for similar materials and temperature [2,9]. This similarity suggests that the non-supplied energy is generated inside the sample, as consequence of the hydride growth, and can be expected to be produced by $Zr + xH \rightarrow ZrH_x$ and $ZrH_x + (2-x)H \rightarrow ZrH_2$ reactions.

Another parameter obtained directly from the difference of voltage in the center is the electrical resistance. This parameter is plotted in Fig. 6. It is interesting to note that the electrical resistance still grows once the reference temperature is stabilized. The slope of the curve begins to decrease when the power drop takes place (see Fig. 4) and it saturates before the dissipated power deficiency reaches its maximum. The general behavior of the curve is similar to the resistivity curve obtained for the phase change $\alpha\text{-}Zr \rightarrow \alpha\text{-}Zr + \delta\text{-}ZrH_{1.5}$ when it is measured in a cylindrical geometry at 700 K [10]. In the first increasing stage both results follow the same behavior and similar values of the relative resistance change attributed to the H dilution in the α-Zr phase. Using this curve as a reference, the observed resistance change corresponds to ≈93 ppm in weight of

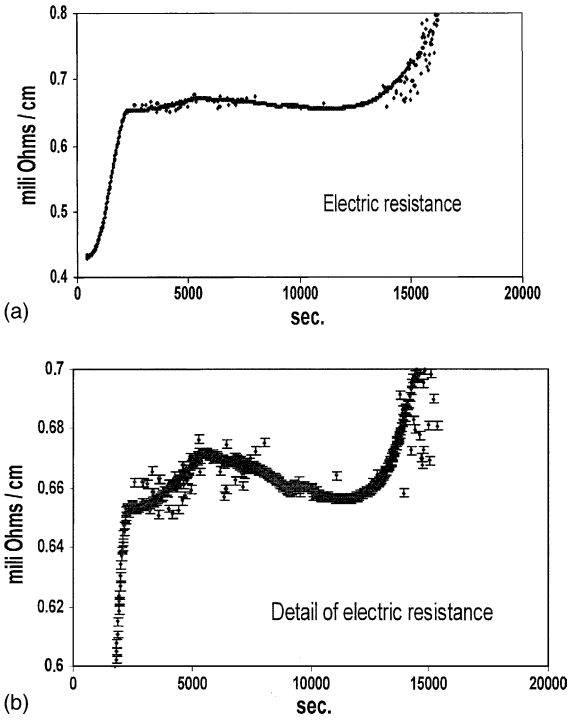


Fig. 6. Electrical resistance in the cladding center during the hydriding. The first increase corresponds to the resistance change due to the temperature increase until the experiment temperature of 360 °C is reached (a). The second positive lower slope corresponds to the H dilution in the α-Zr phase (b). The maximum indicates that the transition $\alpha\text{-}Zr \rightarrow \alpha\text{-}Zr + \delta\text{-}ZrH_{1.5}$ has been initiated.

dissolved H. By taking into account the resistance change per atomic fraction at 603 K, reported in the pioneering work of Mishima et al. [11], a H concentration of 150 ppm can be estimated. In both cases this point is close to the limit of terminal (or maximum) solid solubility (TSS) ≈110 ppm for hydrogen for different Zr alloys measured at 633 K [12–14]. Following the concepts of terminal solid solubility precipitation (TSSP) and terminal solid solubility dissolution (TSSD) and supposing in our case a similar ratio of the concentration values of both limits for different Zr alloys [12,15], a super-saturating value $\leqslant 1.5$ of TSS must be expected for 633 K in the cladding before the start of H precipitation. In summary, it can be stated that the increase in resistance up to the maximum is due to the hydrogen dissolution, and that this maximum indicates when hydrides start to precipitate.

Fig. 7 shows the partial pressure of desorbed $H_2$ from the external surface. The recent work of Sheleifman et al. [7] reports that the thermal desorption curves fit second order kinetics. This means that the desorption value is proportional to $[H]^2$ in the material near the outer surface. The high value of the diffusion coefficient of H in Zr and the formation of a massive hydrided rim as we will show in Fig. 9 (and have been previously reported as a hydride layer on flat samples by Meyer et al. [16]) indicates that this hydrogen concentration corresponds to the H dissolved in the metallic external area of the cladding which is still not invaded by the bulk hydride. From this point of view, the Fig. 7 curve can be interpreted coherently. This desorption curve shows a maximum, whose height ranges in different experiments from nearly 0% up to 100% in relation to subsequent pressure values. When the maximum is not observed, it is substituted by a decrease of the pressure slope. In any case, both alternative features appear at the same time that the resistance maximum, indicating that the H

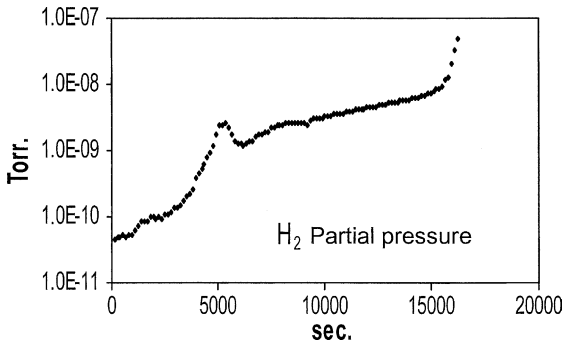


Fig. 7. Partial $H_2$ pressure during the hydriding process. The first maximum corresponds to a residual out-gassing, the following slope is due to the desorption, in $H_2$ form, of H dissolved in the cladding in the α-Zr phase. The maximum indicates that the H precipitation has started. The latter quick slope precedes the immediate tube failure.

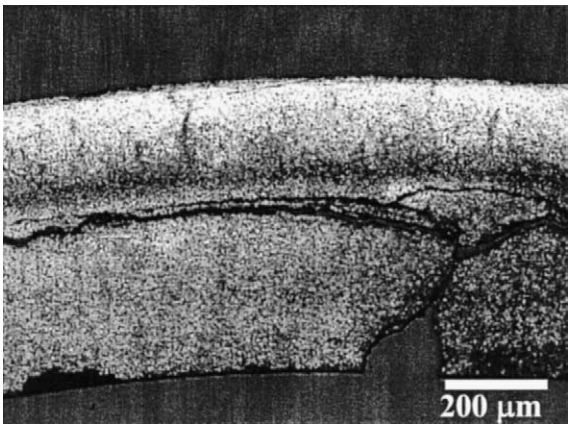


Fig. 8. Optical micrograph of the microstructure resulting after a catastrophic hydriding test. The brittle hydride rim (dark zone), with a thickness of about 400 μm, and the radial hydrides can be observed. Note the circular crack produced by the compressive residual stresses remaining in the hydride layer.

concentration in the metallic Zircaloy suffers a drop or it is slowed down when the transition α-Zr → α-Zr + δ-$ZrH_{1.5}$ takes place. At this stage the hydride rim has been formed and the two phase components, hydride and metallic alloy, appear separated by a clearly defined interface, as Fig. 9(b) shows.

Two non-excluding interpretations of the maximum can be proposed: (i) the maximum and its intensity is a consequence of the H super-saturation, which is reached before precipitation. This super-saturation value depends locally on the material history and its structural details [14,16] giving rise to an augmentation of the intrinsic incoherence in time and position of the H precipitation phenomenon. Therefore, the hydride precipitation can start with different time delays at different zones of the temperature plateau, causing the scatter on the maximum intensity values. (ii) Additionally the maximum can be produced or enhanced by local temperature overheating produced by the high rate of dissipated power that the precipitation start generates, as it is shown in Fig. 4. In any case, this increase of pressure indicates a local instability introduced in the cladding due to the quick start of the hydride precipitation at the inner surface. After the maximum, or the slope change, the $H_2$ partial pressure increases slowly before the last quick slope up. This partial pressure rise corresponds to about 90%, of the hydrogen concentration at the outer surface. The causes of the $H_2$ pressure increase can be explained by several compatible ways: the increase of active centers at the surface for the $H_2$ desorption [7], producing acceleration of the second order kinetics, or an increase in the dissolved [H] due to a change of the mechanical strains distribution. The desorption from a relative small density of hydrides, precipitated at the outer surface, cannot be excluded as an additional $H_2$

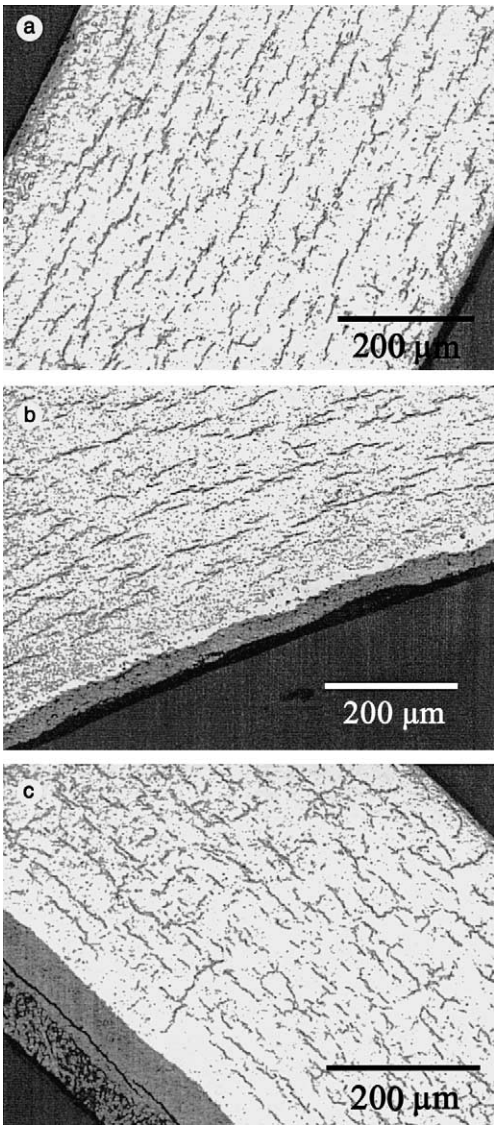


Fig. 9. Micrographs showing the microstructures obtained after different controlled hydriding experiments. (a) Without hydride rim showing circular hydride precipitates. (b) With a hydride layer of ~45 μm in thickness. The orientation of the hydride precipitates remains unchanged. (c) With a hydride rim of ~115 μm in thickness, hydride precipitates with a radial orientation can be observed. This fact indicates that the hydride layer thickness can affect to the hydride precipitates orientation.

source. The last quick slope before the failure time indicates a fast change on the surface and near surface bulk properties of the cladding. The final point in the pressure curve of Fig. 7 precedes the tube failure in less than 60 s. The achieved ultimate morphology can be seen in Fig. 8. The amount of precipitated hydrides decreases uniformly from the hydride layer front to the outer surface of the tube, growing in the radial direction. The brittle fracture observed in the samples is produced by the induced internal stresses due to the volume expansion that takes place around the Zr-hydrides formed in Zircaloy, because the Zr-hydride molar volume is larger than that of Zircaloy. Hydride phases were identified by means of X-ray diffraction. At this advanced hydriding stage, the Zr-hydride layer predominantly consists of ε-$ZrH_2$ and δ-$ZrH_{1.5}$ and no peaks corresponding to zirconium were observed. Conversely, in the sample's outer surface only diffraction peaks for zirconium metal were observed, showing that hydrides are present in minimal amounts at the outer surface, in agreement with the optical observations. The circumferential crack propagated along the hydride layer suggests that this brittle phase must be under compressive stresses, due to the volume expansion, whilst the outer region, hydrided in a lesser extent, should be probably under tensile stresses, promoting the hydride precipitation along the radial direction.

From these results, it can be inferred that the electrical resistance, the power and the pressure curves describe a hydriding process. Considering that the time at which the energy drop starts the incubation time, the power deficiency corresponds to the hydriding dissipated power (HDP), and the electrical resistance increase is related to the hydrogen dissolved in the α-Zr phase until the hydride rim is formed. These facts were confirmed by the analysis of partially hydrided samples.

Therefore, several characteristic parameters of the hydriding process can be measured: the maximum change of resistivity that corresponds to the beginning of the phase change, the incubation time, the failure time and the HDE before the failure. Table 1 shows the results obtained for four samples with the same composition and structure coming from two different fabrication batches. It is very interesting to observe in Table 1 that the failure times and the HDEs are almost the same values in all the cases. Some differences exist in the resistance change, indicating a difference between the

Table 1
Incubation time (ti), failure time (tf), resistivity change (%ro) and HDE for four Zircaloy samples coming from two different batches

| Sample | A1 | A2 | B1 | B2 |
|---|---|---|---|---|
| ti sec. | 2200 | 1640 | 680 | 1080 |
| tf sec. | 14 060 | 12 880 | 14 780 | 14 960 |
| %ro | 0.025 | 0.028 | 0.025 | 0.023 |
| Joules/cm | 1040 | 1018 | 1040 | 1176.66667 |

two batches in the solubility limit before precipitation. It is well known that this value depends on subtle changes in sample processing and history. The incubation time appears reasonably reproduced for the reference temperature (360 °C). This value is usually associated with the surface structure and other composition details, like native oxide layer thickness as well as small water vapor contamination in the $H_2$ line. Several partially hydrided claddings where obtained at 350 °C using the HDP and resistance curves as a reference and assuming that the HDE is mainly related with the hydride rim thickness. The tube cladding sections at three different and significant hydriding stages are shown in Fig. 9. The hydriding dissipated power, the hydriding dissipated energy, the resistance and $H_2$ partial pressure corresponding to the hydriding stage of the thicker rim, Fig. 9(c), are plotted in Figs. 10–13, respectively. The cross-section micrographs shown in Fig. 9 correspond to: (a) a stage before the $\alpha\text{-Zr} \rightarrow \alpha\text{-Zr} + \delta\text{-ZrH}_{1.5}$ transition and close to the beginning of the hydride precipitation that is determined by the resistance change $\approx$1.7%; (b) a stage before the maximum in the HDP curve on Fig. 10; and (c) a stage after the maximum has been surpassed, this is the last point of Fig. 10. The changes in hydriding front and hydride morphologies are evident. The rim thickness of the different samples and their HDE per unit of hydride volume are included in Table 2.

Some worthy results can be straightforwardly deduced, being in progress an additional structural and micromechanical study. Fig. 9(a) shows the state immediately before the $\alpha\text{-Zr} \rightarrow \alpha\text{-Zr} + \delta\text{-ZrH}_{1.5}$ transition without rim formation, where circular hydrides are homogeneously distributed and present in low density, indicating that hydrides have precipitated during the sample cooling. Fig. 9(b) represents a phase after the beginning of the $\alpha\text{-Zr} \rightarrow \alpha\text{-Zr} + \delta\text{-ZrH}_{1.5}$ transition and shows the formation of the hydriding front at the liner. It is interesting to note its wavy like shape which indi-

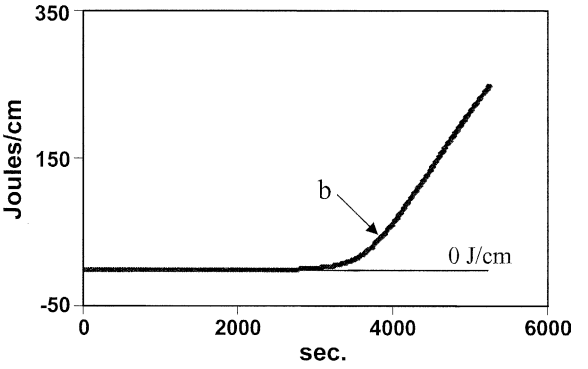


Fig. 11. HDE produced during the formation of the 115 μm hydride rim of Fig. 9(c). The arrow corresponds to hydriding stage of Fig. 9(b).

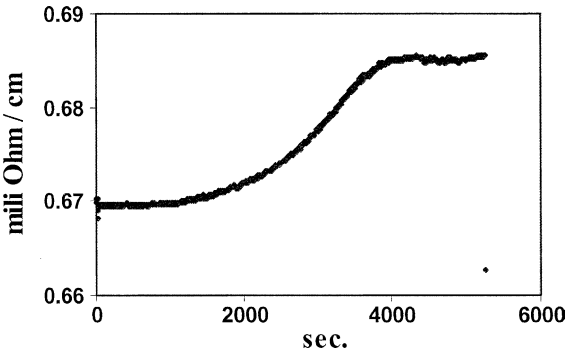


Fig. 12. Electrical resistance in the cladding center during the formation of the 115 μm hydride rim of Fig. 9(c). The increase corresponds to the H dissolution in the α-Zr phase. The maximum indicates that the transition $\alpha\text{-Zr} \rightarrow \alpha\text{-Zr} + \delta\text{-ZrH}_{1.5}$ has been initiated. The time axis starts when the experiment temperature of 350 °C is reached in the center of the tube cladding.

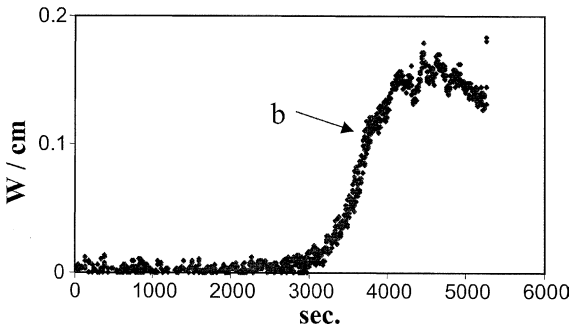


Fig. 10. HDP produced by the hydriding reaction during the growth of the 115 μm hydride rim of Fig. 9(c). The arrow corresponds to the hydriding stage of Fig. 9(b). The time axis starts when the experiment temperature of 350 °C is reached in the center of the tube cladding.

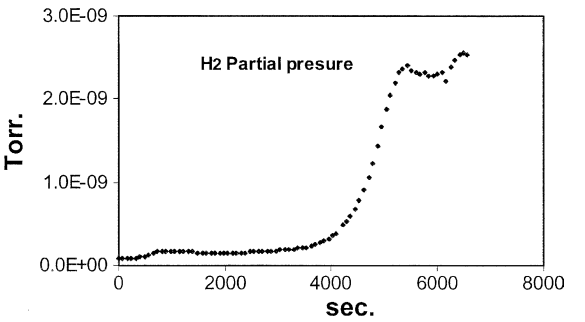


Fig. 13. External partial $H_2$ pressure during the hydriding process corresponding to the rim of Fig. 9(c). The pressure curve show a slope change or a smooth peak at a time close to the maxima of power and resistance of Figs. 10 and 12, respectively.

Table 2
HDE values corresponding to different hydrided rim thickness

| | | | | |
|---|---|---|---|---|
| Thickness mi | 433 | 247 | 133 | 56 |
| Joules/cm$^3$ | 4107 | 3549 | 3372 | 2718 |

cates that the front has been initiated at different points in the inner perimeter and that it has not stabilized yet. The values of the equivalent reaction energy for this sample are marked in Figs. 10 and 11. At this stage, Fig. 10 shows that the energy dissipated by the reaction increases quickly with the time. In the more advanced hydriding stage of Fig. 9(c), the hydride front appears in a circular shape and radial hydrides begin to develop. At this point important mechanical effects begin to take place as the observed circular crack indicates.

Table 2 shows how the HDE per unit of volume increase with the hydride thickness. This HDE increase indicates that different $ZrH_x$ stoichiometries with increasing hydrogen concentration are produced during the hydriding progress. The X-ray analysis of the inner surface of the Fig. 9(b) shows a cubic phase corresponding to $\delta$-$ZrH_2$ or $\delta$-$ZrH_{1.5}$. Both compounds present very close d-spacings and intensity ratios, making it nearly impossible to discriminate between them. However, the increase of energy per volume unit related to the hydride thickness as shown in Table 2, allows us to discard the phase with the maximum amount of H. This is in agreement with the expected phase transition for low H concentrations at the beginning of rim formation. The high rate of HDP at the beginning of precipitation indicates that the analyzed phase is produced in a relatively quick hydriding process.

After the maximum, the HDP decreases with the thickness, in an opposite tendency to the HDE per volume unit. This tendency indicates that the progression of the hydride front decreases during the cladding hydriding. Probably this slow down effect is the consequence of a continuous hydride layer formation with a relatively low H diffusion coefficient. It is interesting to note that the increase in HDP and the wave like front at the onset of the hydride precipitation is in agreement with the hydriding model of Inomata et al. [8].

The present discussion demonstrates that the combination of different measurements during the hydriding tests of Zircaloy tube claddings, similar to those reported in this work, together with cross-sections and structural analyses can give deep insight into the kinetic and structural processes of these nuclear materials.

## 4. Conclusions

An UHV method to study the hydriding of tube claddings from their inner surface has been developed. The method is useful to test the behavior and resistance under this destructive process. The initial application shows that the hydride precipitation takes place in the form of an inner rim with an initial high speed front propagation associated with a shape instability and a relatively low stoichiometry. In a second stage the propagation slows down and the H content of the rim increases.

## Acknowledgements

This study has been financially supported by the CYCIT-IBERDROLA Project No. 95-0268-OP and by the IBERDROLA-WESTINGHOUSE ATOM AB Project HZIRCA II. We would like to thank WESTINGHOUSE and ENUSA for providing different types of samples and Samuel Perez for his initial advice. Especially, we greatly appreciate the advice and comments of Magnus Limbäck, Mats Dahlbäck and Kathleen Terryill. We also thank Eduardo Santamera, José Esteban, Jesús Revilla, José Flores and Miguel Cañas for their technical support.

## References

[1] H.S. Hong, D.R. Olander, J. Nucl. Mater. 297 (2001) 107.
[2] Y.-S. Kim, S.-K. Kim, J. Nucl. Mater. 270 (1999) 147.
[3] Y.S. Kim, W.-E. Wang, D.R. Olander, S.K. Yagnik, J. Nucl. Mater. 246 (1997) 43.
[4] P. Billot, S. Yagnik, N. Ramasubramanian, J. Peybernes, D. Pecheur, 13th International Symposium on Zirconium in the Nuclear Industry (Oral communication and Abstract) 2002.
[5] J.L. Sacedón, E. Santamera, M. Díaz, J.S. Moya, E. Román, A.S. Pérez, B. Remartínez, PCT/ES01/00350, 2003.
[6] J.L. Sacedón, M. Díaz, J.S. Moya, B. Remartínez, J. Izquierdo, Patent no. P200400294, 2004.
[7] D.E. Sheleifman, D. Shaltiel, I.T. Steinberger, J. Alloy Compd. 223 (1995) 81.
[8] A. Inomata, H. Aoki, T. Miura, J. Alloy Compd. 278 (1998) 103.
[9] K. Une, J. Less-Common Met. 57 (1978) 93.
[10] A. Kaneda, M. Yamamoto, S. Naito, M. Mabuchi, T. Hashino, J. Phys. Condens. Matter 18 (1998) 4645.
[11] Y. Mishima, S. Hishino, S. Nakajima, J. Nucl. Mater. 27 (1968) 335.
[12] J.J. Kearns, J. Nucl. Mater. 22 (1967) 292.
[13] D. Khatamian, V.C. Ling, J. Alloy Compd. 253 (1997) 162.
[14] M.P. Puls, Acta Metall. 29 (1981) 1961.
[15] D. Kahatamian, Z.L. Pan, M.P. Puls, C.D. Cann, J. Alloy Compd. 231 (1995) 488.
[16] G. Meyer, M. Kobrinsky, J. Abriata, J.C. Bolcich, J. Nucl. Mater. 229 (1996) 48.